Additive Manufacturing 49 (2022) 102517

Contents lists available at ScienceDirect

Additive Manufacturing

journal homepage: www.elsevier.com/locate/addma

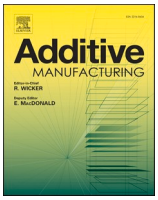

Microstructure evolution and mechanical properties of a high-strength Mg-10Gd-3Y–1Zn-0.4Zr alloy fabricated by laser powder bed fusion

Qingchen Deng [a], Yujuan Wu [a,*], Qianye Wu [a], Yanting Xue [a], Yu Zhang [b], Liming Peng [a], Wenjiang Ding [a]

[a] National Engineering Research Center of Light Alloy Net Forming and State Key Laboratory of Metal Matrix Composites, School of Materials Science and Engineering, Shanghai Jiao Tong University, Shanghai 200240, China
[b] College of Materials Science and Engineering, Chongqing University, Chongqing 400044, China

ARTICLE INFO

Keywords:
Laser powder bed fusion (LPBF)
Mg-Gd-Y-Zn-Zr alloy
Post-processing
Microstructure evolution
Mechanical properties

ABSTRACT

A high-strength Mg-10Gd-3Y–1Zn-0.4Zr (GWZ1031K, wt%) alloy was prepared by laser powder bed fusion (LPBF), and the microstructure and mechanical properties of the as built, LPBF-T5, LPBF-T4, and LPBF-T6 states were systematically studied. The as built alloy is composed of fine equiaxed α-Mg grains with an average grain size of 4.1 ± 0.5 μm, reticular β-$(Mg,Zn)_3(Gd,Y)$ eutectic phase and flaky Y_2O_3 oxide phase, and exhibits yield strength (YS) of 310 ± 8 MPa, ultimate tensile strength (UTS) of 347 ± 6 MPa and elongation (EL) of 4.1 ± 0.8%. A simple direct aging heat treatment at 175 ℃ for 64 h after LPBF leads to an ultra-high YS of 365 ± 12 MPa but a low EL of 0.8 ± 0.3% in the LPBF-T5 alloy. The solution heat treatment improves ductility by transforming the hard and brittle eutectic phase into the relatively soft and deformable lamellar long period stacking ordered (LPSO) structure inside grains and X phase at grain boundaries without obvious grain growth. Moreover, the LPBF-T4 alloy solution-treated at 450 ℃ for 12 h exhibits YS of 255 ± 8 MPa, UTS of 328 ± 9 MPa, and EL of 10.3 ± 0.5%. Aging heat treatment after solution introduces numerous prismatic β′ and β_1 precipitates, which help to increase tensile strength. The YS, UTS, and EL of the LPBF-T6 alloy are 316 ± 5 MPa, 400 ± 7 MPa, and 2.2 ± 0.3%, respectively. It can be concluded that the LPBF process when combined with specially designed post-processing holds great promise for the manufacturing of high-performance components of the Mg-rare earth alloys with significantly higher YS for various applications.

1. Introduction

Magnesium (Mg) alloys have an obvious weight reduction effect when used in automobile, space and aircraft fields owing to the low density, high specific strength, and specific stiffness [1,2]. Mg alloys are also gaining popularity in the biomedical fields due to their good biocompatibility and biodegradability [3]. In order to use Mg alloys as lightweight load-bearing components in many critical engineering fields, pursuing Mg alloys with improved mechanical properties has been an eternal theme. The Mg-Gd series alloys are an essential category of high-performance Mg alloys due to the significant precipitation strengthening effect [4,5]. To further enhance the mechanical properties while reducing the amount of expensive Gd element, Y element is added to Mg-Gd series alloys to promote aging hardening response by generating more precipitates [6]. The addition of Zn element to Mg-RE (rare earth) alloys will introduce long period stacking ordered (LPSO) structure, which can enhance both the strength and ductility [7–9]. Besides, the Zr element is often added to Mg alloys to refine the grains [10]. For example, Liu et al. [11] fabricated a high-strength Mg-9.8Gd-3.2Y-1.1Zn-0.42Zr (wt%) alloy in cast-T6 state with yield strength (YS) and ultimate tensile strength (UTS) of 253 MPa and 364 MPa, respectively. Therefore, Mg-Gd series alloys with the appropriate addition of Y, Zn and Zr elements will be a potential high-performance Mg alloy.

At present, Mg alloy components are mainly prepared by die-casting [12], permanent mold [13,14], or sand mold [15,16] casting methods. The disadvantages of these methods are inevitable casting defects such as porosity, inclusion and segregation, undesirable mechanical properties, low manufacturing accuracy and extremely long developing cycles, which restrict the practical application of Mg alloys. Thus, novel manufacturing technologies are desperately required to fabricate high-performance Mg alloy components.

* Corresponding author.
E-mail address: wuyj@sjtu.edu.cn (Y. Wu).

https://doi.org/10.1016/j.addma.2021.102517
Received 5 September 2021; Received in revised form 4 November 2021; Accepted 25 November 2021
Available online 27 November 2021

With the growing trend of industrial intelligence and pollution reduction, laser powder bed fusion (LPBF), the most hopeful metal additive manufacturing (AM) technology, has great potential for fabricating high-performance Mg alloy components with complex shapes to replace conventional casting methods [17,18]. The extremely fast cooling rate of the LPBF process (~10^5 K/s) [19] contributes to rapidly solidified non-equilibrium microstructure with fine grains, so the as built samples often possess higher tensile strength than their cast counterparts owing to the significant fine grain strengthening effect [20–22]. However, the as built samples usually have large residual stress due to the rapid heating and cooling cycles that occur throughout the manufacturing process [23]. Thus, deformation or even cracks occur in the as built samples when the degree of their deformation exceeds the ductility [24,25]. Post-processing of the as built samples is required to relieve residual stresses and improve their mechanical properties. For instance, Liu et al. [26] performed hot isostatic pressing (HIP) on the as built AZ61 Mg alloy, and the elongation was found to be significantly improved due to the closure of pores while the micro-hardness and tensile strength decreased owing to the growth of grain size after HIP. It is essential to avoid excessive grain growth and dissolve the hard and brittle eutectic phase simultaneously during the high temperature treatment. Therefore, the solution heat treatment condition should be redesigned according to the unique microstructure of the as built alloys. The aging heat treatment after solution can produce numerous aging precipitates leading to significant precipitation strengthening [4,5,15], which is essential to fabricate high-strength Mg-Gd-Y series alloys.

Nowadays, metals such as Al alloys (AlSi10Mg [27]), Ti alloys (Ti–6Al–4V [28]), Ni-based alloys (Inconel 718 [29]), Fe-based alloys (316L stainless steels [30]) have been successfully manufactured by LPBF with high relative density and excellent mechanical properties. However, the LPBF of the Mg alloys is extremely difficult due to the high explosion tendency of Mg powder, the high saturated vapor pressure and the low boiling point of the Mg [17,18]. So far, LPBF has been only applied to pure Mg [20,31,32] and traditional commercial cast Mg alloys containing Mg-Al series [33–40], Mg-Zn series [24,25,41–43], and WE43 alloys [44–48]. Wei et al. [36] optimized the LPBF process parameters for AZ91D alloy resulting in a high relative density of 99.52%, and the micro-hardness and tensile strengths of the as built AZ91D alloy were better than that of the die-cast alloy. Shuai et al. [42] fabricated ZK60 alloy using LPBF and discovered that the refined grains, homogeneously distributed Mg_7Zn_3 secondary phase, and extended solid solution of alloying elements induced by laser rapid solidification can improve hardness and corrosion resistance. Bar et al. [47] conducted a detailed microstructure analysis of biodegradable WE43 alloy and identified three different types of microstructures (equiaxed zone, lamellar zone and partially melted zone) in one molten pool. Recently, Wang et al. [49], for the first time, studied the effect of the geometrical design on the dynamic compressive properties and dynamic biodegradation behavior of the as built Mg-3Nd-0.2Zn-0.4Zr (wt%) alloy for orthopedic applications. In our previous work [22], an Mg-Gd-Zn-Zr alloy was prepared by LPBF, and the influence of process parameters on formability, element vaporization, mechanical and room temperature tensile properties of the as built alloy was systematically investigated. However, no research has been conducted on the formability, the evolution of microstructure and mechanical properties of high-strength Mg-Gd-Y-Zn-Zr alloys prepared by LPBF from the as built state to the solution-treated and aging-treated states.

In this work, a high-strength Mg-10Gd-3Y–1Zn-0.4Zr (GWZ1031K, wt%) alloy was prepared by LPBF and post-processing. The evolution of microstructure and mechanical properties from the as built state to the solution-treated (LPBF-T4) and aging-treated (LPBF-T6) states were systematically studied. The secondary phases in the as built, solution-treated and aging-treated states were characterized in detail. The influence of heat treatment on microstructure evolution and mechanical properties of the high-strength GWZ1031K alloy was explored, and the underlying strengthening mechanism was clarified.

2. Experimental details

Initially, the semi-continuous casting method was used to fabricate GWZ1031K ingot with a diameter of 110 mm. Then GWZ1031K pre-alloyed powder was obtained by remelting semi-continuous ingot and subsequent centrifugal gas atomization process (Tangshan Weihao Magnesium Powder Co., LTD, China). Finally, ZRapid iSLM 150 3D printer (ZRapid Tech Co., LTD., China) was adopted to fabricate the as built GWZ1031K alloy. Two different series of specimens were printed: cubes with a size of 10 mm × 10 mm × 10 mm were prepared for microstructure characterization and bone-shaped specimens with gauge size of 18 mm × 3 mm × 10 mm were built for tensile tests. Based on the LPBF process parameters optimized for Mg-Gd series alloy [22], the LPBF process parameters used in this work are displayed in Table 1. The island scanning strategy with island width of 5 mm and bi-directional scanning were employed to weaken stress accumulation. A large number of evaporative fumes (Fig. 1a) were noticed during the entire LPBF process owing to the low boiling point (~1093 ℃) and high saturated vapor pressure of Mg [50]. The violent powder splashing only occurs during the LPBF process of metals with low boiling points such as Mg and Zn alloys [51], which will affect the stability of the LPBF process and change the chemical compositions of the as built alloy. The evaporative fumes cannot be eliminated by the cyclic Ar, and some of them remain above the scanning area during the printing process. The remaining fumes above the scanning area reflect the laser energy, and as a result, laser energy becomes unstable. Too high or too low laser energy will cause defects such as pores and macro cracks. Besides, evaporative fumes will result in a higher layer thickness than the preset, making it more prone to defects. The violent powder splashing will create depressions in the laser scanning area. To ensure that the entire build platform could be covered with enough powders after scanning one layer, the rising height of the powder bed (the powder supply of each layer) was kept 3 times the layer thickness. Alloying treatment can effectively increase the gap between melting point and boiling point [52], and increasing the pressure in the build chamber can increase the boiling point of Mg alloys [32], both of which are helpful to weaken evaporation. Furthermore, a lower laser energy density will lower the temperature of the molten pool leading to reduced evaporation. Macro cracks (Fig. 1b) can be occasionally observed at the side plane (XOZ plane) of the as built samples, so only the samples with a thickness of 1.5 mm and free of macro cracks were selected to perform the tensile test.

Despite the very high cooling rate of the LPBF process, the as built GWZ1031K alloy still contains a network of hard and brittle eutectic phases that is very harmful to ductility, so solution heat treatment is necessary to dissolve the eutectic phase. The maximum solid solubility of Gd and Y elements in α-Mg matrix are 23.5 wt% and 12.5 wt%, respectively. Because solid solubility decreases sharply as the temperature decreases, Mg-Gd-Y series alloys exhibit significant solid solution strengthening and precipitation strengthening [1,2]. Aging heat treatment after solution is also necessary to produce nano-sized aging precipitates, because precipitation strengthening is a major strengthening mechanism for high-strength Mg-Gd series alloys [1,4,5]. Therefore, the as built GWZ1031K alloy further underwent post-processing including solution and aging heat treatments to modify the microstructure and improve mechanical properties. A small amount of pyrite (FeS) was put

Table 1
The LPBF process parameters.

Parameters	Value
Laser power (W)	80
Scanning speed (mm/s)	200
Hatch spacing (μm)	100
Layer thickness (μm)	30
Preheating temperature of build platform and powder bed (℃)	100
Oxygen and water vapor content (ppm)	< 100
Hatch angle (°)	67

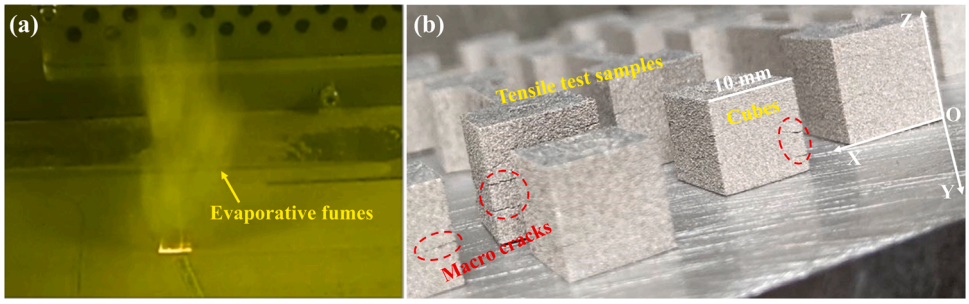

Fig. 1. (a) Evaporative fumes during the LPBF process and (b) side view of the as built GWZ1031K samples where red ovals indicate macro cracks.

into a muffle furnace to avoid ignition and oxidation of Mg alloy samples by generating SO_2 protective gas during the heating process. Then the solution-treated GWZ1031K alloy was artificially aged at 175 ℃ or 200 ℃ from 0 h to 512 h in an oil bath (LPBF-T6). Vickers hardness testing with a load of 49 N and a residence time of 15 s was conducted to analyze the aging hardening response. Each hardness value is the average of at least five measurements.

All microstructure characterization was conducted on the side plane of the cubes parallel to the building direction (BD, Z direction) of the LPBF process because the side plane contains fish-scale-shaped molten pools. For optical microscopy (OM) and scanning electron microscope (SEM) observations, the samples were etched in the acetic-picral solution (4.2 g picric acid, 10 mL acetic acid, 80 mL ethyl alcohol, and 10 mL water) after being mechanical ground by SiC abrasive papers (#320, #1200, #3000, #7000) and then polished with nano magnesium oxide (≤50 nm) suspension. The specific details of inductively coupled plasma atomic emission spectroscopy analyzer (ICPAES), SEM (TESCAN MIRA3) equipped with an energy dispersive X-ray spectrometer (EDS), X-ray diffraction (XRD, Poly-functional X-Ray Diffractometer), OM (Zeiss Axio observer), electron backscatter diffraction (EBSD, TESCAN GAIA3), transmission electron microscope (TEM, FEI TECNAI G^2 S-TWIN), average grain size (linear intercept method, ASTM E112–12) and porosity measurement, and room temperature tensile tests (Zwick/Roell Z100 material test machine) were the same as in our previously published work [22,53,54].

3. Results

3.1. Powder characterization

The measured chemical compositions of the ingot, powder, and as built GWZ1031K alloy are displayed in Table 2. The content of alloying elements in the powder is close to that of ingot, while the content of alloying elements in the as built alloy is slightly higher than that of powder, indicating a more severe vaporization loss of Mg compared with alloying elements during the LPBF process [22,41].

The 200–300 mesh powder with a mean particle diameter of 63.9 μm was used in the present study, whose particle size distribution can be found in reference [53]. Fig. 2 presents the morphology and microstructure of the GWZ1031K pre-alloyed powder. Most of the powder particles are spherical while some satellite powder particles indicated by yellow arrows and irregular-shaped powder particles indicated by white arrows can be observed despite the sieving process (Fig. 2a). Lots of fine white particles with a diameter of hundreds of nanometers appear on the surface of the powder (Fig. 2b). As shown in Fig. 2c, the pre-alloyed powder contains a fine α-Mg matrix and reticular eutectic phase on grain boundary. According to the ASTM E112–12, the average grain size of the GWZ1031K pre-alloyed powder is 2.1 ± 0.8 μm. Based on EDS maps (Fig. 2d), the white particles on the surface of the powder are presumably oxide particles. The phase constitution of the GWZ1031K pre-alloyed powder will be identified by XRD.

Table 2
The measured chemical compositions of the ingot, powder, and as built GWZ1031K alloy (wt%).

Materials	Gd	Y	Zn	Zr	Mg
Ingot	10.88	2.46	0.95	0.43	Bal.
Powder	11.02	2.41	0.96	0.40	Bal.
As built alloy	11.82	2.58	1.06	0.43	Bal.

3.2. Phase analysis

Fig. 3 reveals XRD patterns of the pre-alloyed powder, as built, LPBF-T4, and LPBF-T6 GWZ1031K alloys. The pre-alloyed powder contains α-Mg matrix and β-$(Mg,Zn)_3(Gd,Y)$ eutectic phase while the oxide particles are not detected due to relatively low content. The as built alloy includes α-Mg matrix, β-$(Mg,Zn)_3(Gd,Y)$ eutectic phase, and undesired Y_2O_3 oxide phase, suggesting that slight oxidation occurred during LPBF. After solution heat treatment, the eutectic phase is completely transformed into a LPSO structure, resulting in the LPBF-T4 alloy containing three phases: α-Mg matrix, LPSO structure, and Y_2O_3. The phase constitution of the LPBF-T6 alloy is identical to that of the LPBF-T4 alloy except for aging precipitates. XRD cannot be determined aging precipitates, so they will be identified in Section 3.5.

3.3. Microstructure of the as built alloy

Fig. 4 presents OM and BSE-SEM images of the as built GWZ1031K alloy. Despite using the optimized LPBF process parameters, there are still numerous circular pores (Fig. 4a) and no irregular-shaped lack of fusion defects. The highly concentrated laser energy causes the temperature of the molten pool to quickly reach the boiling point (~1093 ℃) of Mg, but the Mg vapor cannot escape from the molten pool due to the ultra-fast solidification rate, resulting in the formation of circular pores [55]. The porosity including cracks of the as built alloy is 2.15 ± 0.11%, which is close to that of the as built AZ61 alloy (2%) [39] and pure Mg (2.5%) [31]. Besides, large cracks (Fig. 4a) parallel to the scanning direction (SD) of LPBF process are found in the as built alloy, which cannot be eliminated just by adjusting laser energy density. Cracks are classified into two categories: hot cracks and cold cracks. Hot cracks are primarily composed of solidification cracks, which are formed in the final stage of the solidification process as the liquid film on the grain boundary is being pulled apart by thermal stresses [24,25]. Cold cracks are formed after the end of solidification when the thermal stress exceeds the ultimate strength of the material or the strain caused by solidification shrinkage and thermal shrinkage exceeds the ductility of the material [56,57]. The macro cracks in the as built GWZ1031K alloy are different from solidification cracks found in the as built Mg-Zn series alloys [24,25] and high-strength Al alloys [58,59], because the direction of solidification cracks is mostly parallel to the BD of the LPBF process. Additionally, solidification cracks are usually micro cracks evenly distributed throughout the as built sample, while cold cracks are relatively macro cracks concentrated at a certain height. More importantly,

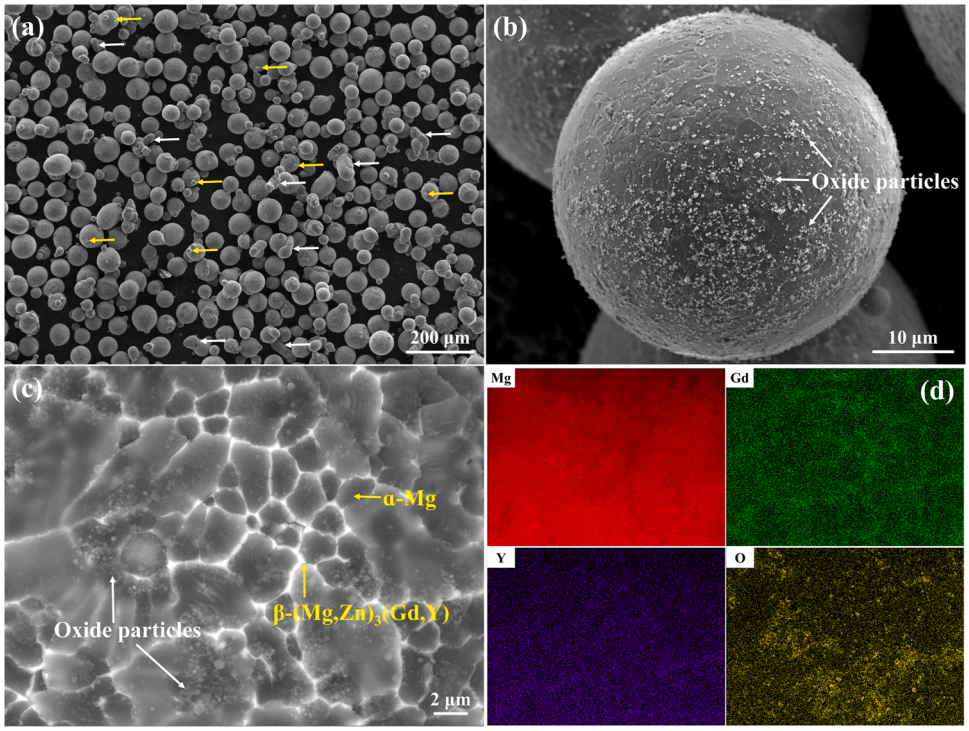

Fig. 2. The overall morphology (a), SE-SEM micrograph (b), BSE-SEM micrograph (c) and corresponding EDS maps (d) from (c) of the GWZ1031K pre-alloyed powder.

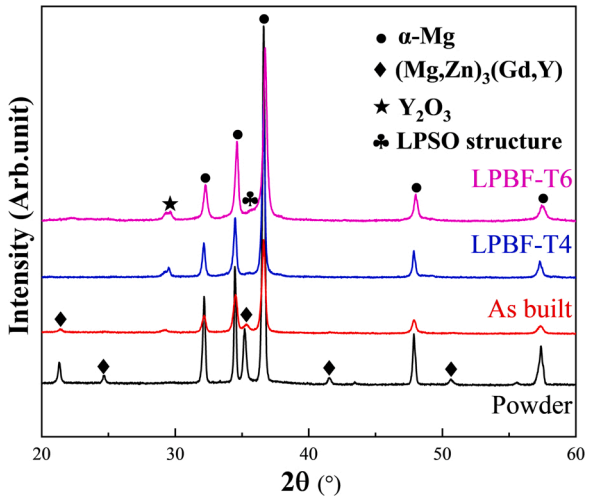

Fig. 3. XRD patterns of the pre-alloyed powder, as built, LPBF-T4, and LPBF-T6 GWZ1031K alloys.

there are no cracks in the upper area of the as built GWZ1031K cubes, indicating that cracking does not occur during the solidification of the molten pools. The as built GWZ1031K cube has cracks at a certain height, but no cracks in the upper and lower areas of the existing cracks. As the printing process progresses, cold cracks will be formed after the thermal stress or strain accumulates to a certain degree. The thermal stress or strain is released after the cold cracks are formed, so there are no more cracks on the upper area of the cold cracks until a new cold crack is formed. Increasing the height or the area of the part will increase the number of cold cracks. Consequently, the macro cracks in the as built GWZ1031K alloy are most likely cold cracks. To eliminate the cracks, the build platform is preheated to 400–500 ℃ to reduce the temperature gradient that contributes to small thermal stress or change chemical composition to one that is more ductile to resist greater deformation.

One representative fish-scale-shaped molten pool with the molten pool boundary indicated by yellow dotted lines and many hexagonal equiaxed dendrite grains [60] indicated by yellow arrows (Fig. 4b) can be observed. Outside the molten pool, some dot-shaped $(Mg,Zn)_3(Gd,Y)$ secondary phases are distributed inside the grains (Fig. 4c), because the thermal effect from the inside of the molten pool leads to the precipitation of the secondary phase. As displayed in Fig. 4d, the as built GWZ0131K alloy consists of gray α-Mg matrix and bright reticular β-$(Mg,Zn)_3(Gd,Y)$ eutectic phase at grain boundaries with an area fraction of 7.78 ± 0.15%.

Fig. 5 shows BSE-SEM image and corresponding EDS maps of oxides in the as built GWZ1031K alloy. EDS results show that the flaky white phases are enriched in Y and O elements, suggesting the existence of Y_2O_3 oxides, which is in good agreement with the XRD patterns. The affinity of Y to O is greatest among other alloying elements and Mg [45].

Fig. 6 reveals the inverse pole figure (IPF), image quality (IQ) map, grain size distribution and pole figure of (0001) plane in the as built GWZ1031K alloy. The as built GWZ1031K alloy is composed of relatively uniform equiaxed grains with various crystal orientations and no large columnar grains (Fig. 4a-b) due to the high content of alloying elements, especially enough Zr element for heterogeneous nucleation sites causing high values of growth restriction factor [61]. The average grain size of the as built alloy is just 4.1 ± 0.5 μm (Fig. 4c). The pole figure of (0001) plane has a centralized distribution (Fig. 4d), but the maximum intensity of texture is as low as 2.813 mud (multiple uniform distribution). Therefore, the as built GWZ1031K alloy is homogeneous and isotropic.

Fig. 7 displays bright-field TEM images of basal γ′ precipitates in the as built GWZ1031K alloy. Adding Zn to Mg-Gd-Y series alloys leads to co-segregation of rare earth atoms (Gd and Y atoms) and Zn atoms, which is necessary for the formation of basal γ′ precipitates with an orderly stacking sequence of ABCA [5]. The orientation relationships between α-Mg and γ′ precipitates are $(0001)_{\gamma'}$ // $(0001)_{\alpha\text{-Mg}}$ and $(2\bar{1}\bar{1}0)_{\gamma'}$ // $(2\bar{1}\bar{1}0)_{\alpha\text{-Mg}}$ [62]. Although there is no lamellar 14H-LPSO structure in the as built GWZ1031K alloy, 14H-LPSO structure may be transformed from γ′ precipitates during solution heat treatment, because basal γ′

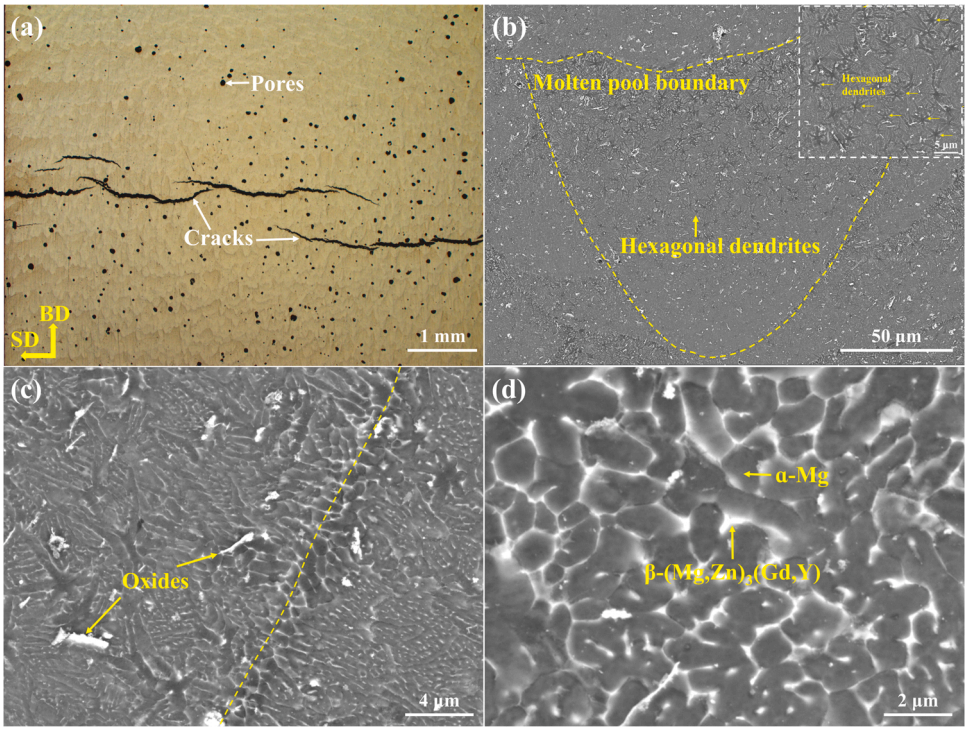

Fig. 4. OM (a) and BSE-SEM (b-d) images of the as built GWZ1031K alloy.

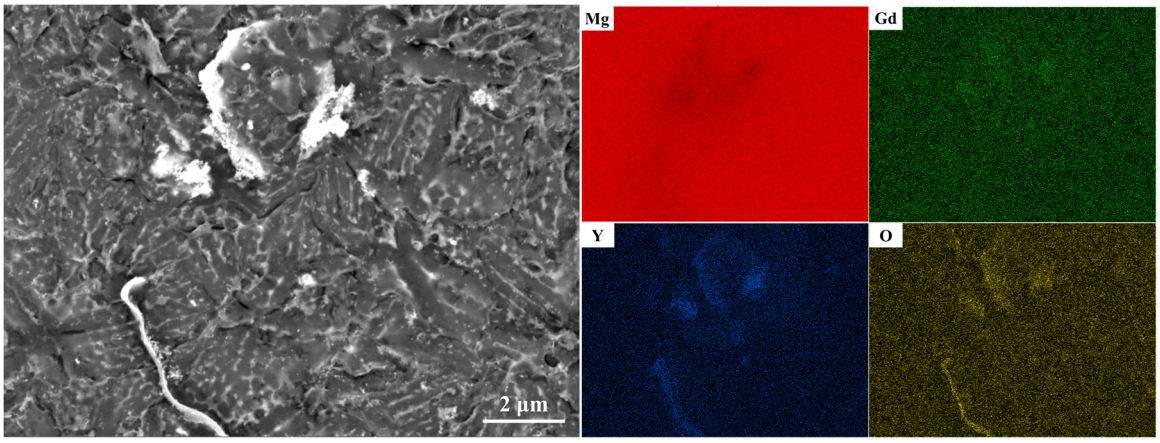

Fig. 5. BSE-SEM image and corresponding EDS maps of oxides in the as built GWZ1031K alloy.

precipitates are the basic unit of 14H-LPSO structure and high temperature can promote the diffusion of atoms.

3.4. Solution heat treatment

Fig. 8 exhibits BSE-SEM images of the as built GWZ1031K alloy solution-treated at 500 ℃ for different time. The eutectic phase in the cast GWZ1031K alloy can be completely dissolved after solution heat treatment at 500 ℃ for 10 h [11]. However, the eutectic phase in the as built GWZ1031K alloy completely transforms into lamellar LPSO structure inside grains and X phase at grain boundaries only after a short-term solution heat treatment at 500 ℃ for only 1 h (Fig. 8a-b). Extremely fine grains significantly shorten the diffusion distance of atoms and less content of the eutectic phase in the as built alloy promotes the dissolution of the eutectic phase. With the increase of solution time, lamellar LPSO structure at grain interior becomes denser and grain growth occurs.

Fig. 9 presents the room temperature tensile properties of the as built and solution-treated GWZ1031K alloys at 500 ℃ for different time. The YS of the solution-treated GWZ1031K alloy is smaller than that of the as built alloy because the hardness and Young's modulus of the eutectic phase are larger than that of lamellar LPSO structure and X phase contributing to a stronger strengthening effect [8,63], the residual stress is released and the grain growth occurs after solution heat treatment. Nevertheless, the eutectic phase is particularly brittle, and the area fraction of eutectic phase is as high as 7.78 ± 0.15%, which will severely deteriorate ductility. As a result, solution heat treatment is necessary to transform the hard and brittle eutectic phase into a relatively soft and deformable LPSO structure, and subsequent aging heat treatment compensates for the loss of strength caused by solution heat treatment. With the increase of the solution treatment time, YS of the solution-treated alloy decreases owing to grain growth. Both tensile strengths (YS and UTS) and ductility (EL) of the as built GWZ1031K alloy solution treated at 500 ℃ for 1 h are highest among other solution treatment time.

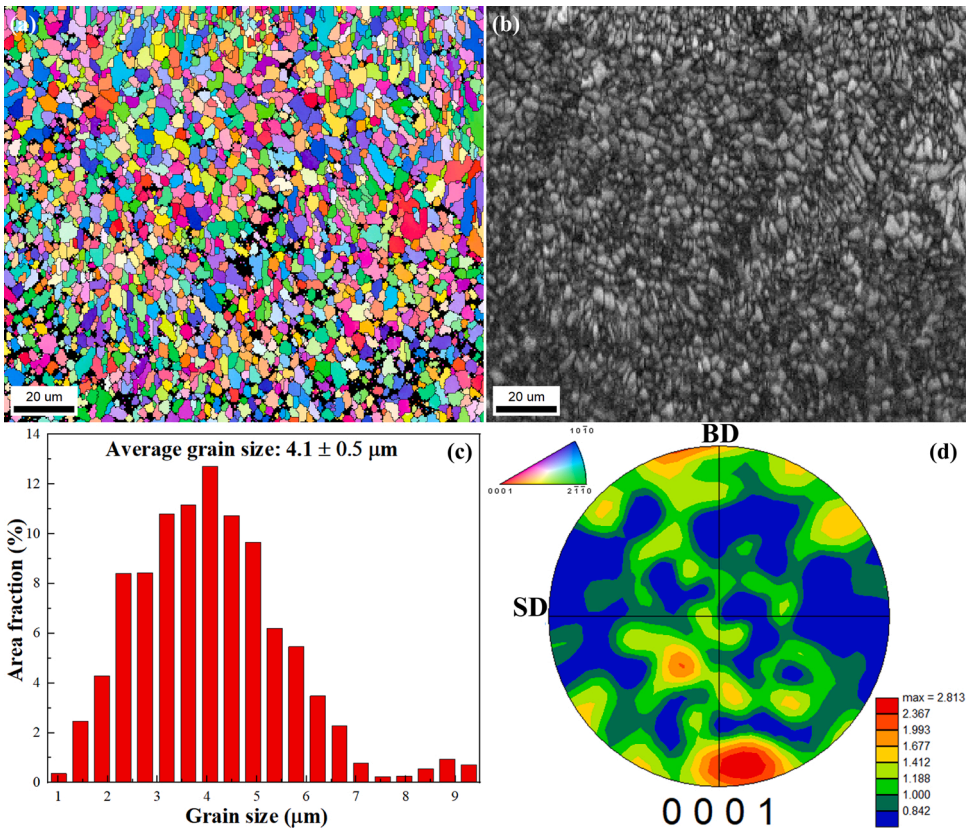

Fig. 6. EBSD observations of the as built GWZ1031K alloy: (a) IPF, (b) IQ map, (c) grain size distribution, (d) pole figure of (0001) plane.

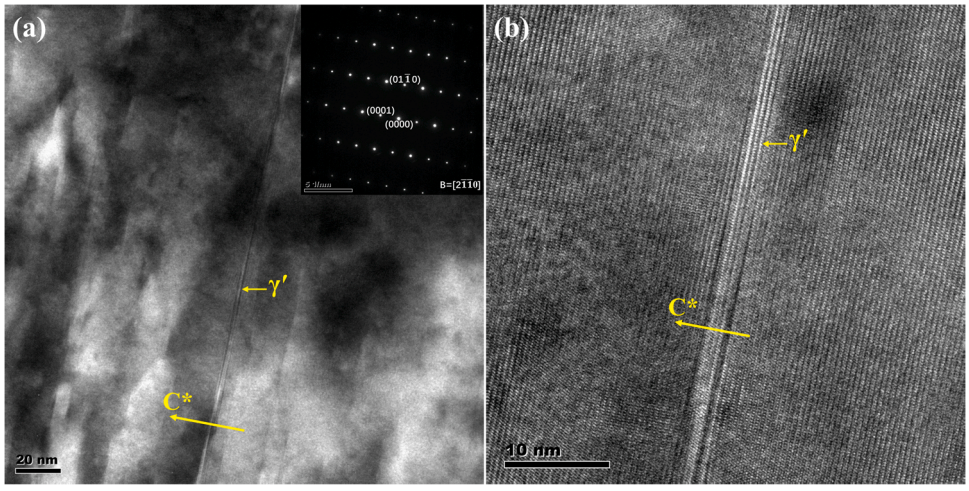

Fig. 7. Bright-field TEM images of basal γ′ precipitates in the as built GWZ1031K alloy.

Therefore, the best solution treatment time at 500 ℃ for the as built GWZ1031K alloy is 1 h. The LPBF-T4–1 GWZ1031K alloy is defined as the as built GWZ1031K alloy solution treated at 500 ℃ for 1 h.

In addition, solution heat treatment needs to be redesigned considering the peculiar solidification conditions of LPBF [64], so a lower solution temperature of 450 ℃ is also adopted. Fig. 10 presents BSE-SEM images of the as built GWZ1031K alloy solution treated at 450 ℃ for different time. Lower temperature at 450 ℃ can also transform the eutectic phase into lamellar LPSO structure inside grains and X phase at grain boundaries. This type of solid state transformation only belongs to Mg-Gd-(Y)-Zn series Mg alloys, where LPSO structure was frequently reported as an important strengthening phase [7,8,11]. The lamellar LPSO structure in solution-treated GWZ1031K alloy at 450 ℃ is denser than that of 500 ℃, which will contribute more to the YS.

Fig. 11 shows the room temperature tensile properties of the as built and solution-treated GWZ1031K alloy at 450 ℃ for different time. At the same solution time, both the YS and EL of solution-treated GWZ1031K alloy at 450 ℃ are higher than that of 500 ℃, which indicates that 450 ℃ is a better solution temperature. YS decreases approximately linearly with the increase of solution treatment time at 450 ℃. As the solution time extends from 1 h to 12 h, the YS only decreases slightly (from 265 MPa to 255 MPa) due to the relatively short solution time. However, as the solution time further increases to 24 h or 36 h, the YS drops dramatically to 242 MPa or 235 MPa, respectively. The solution-

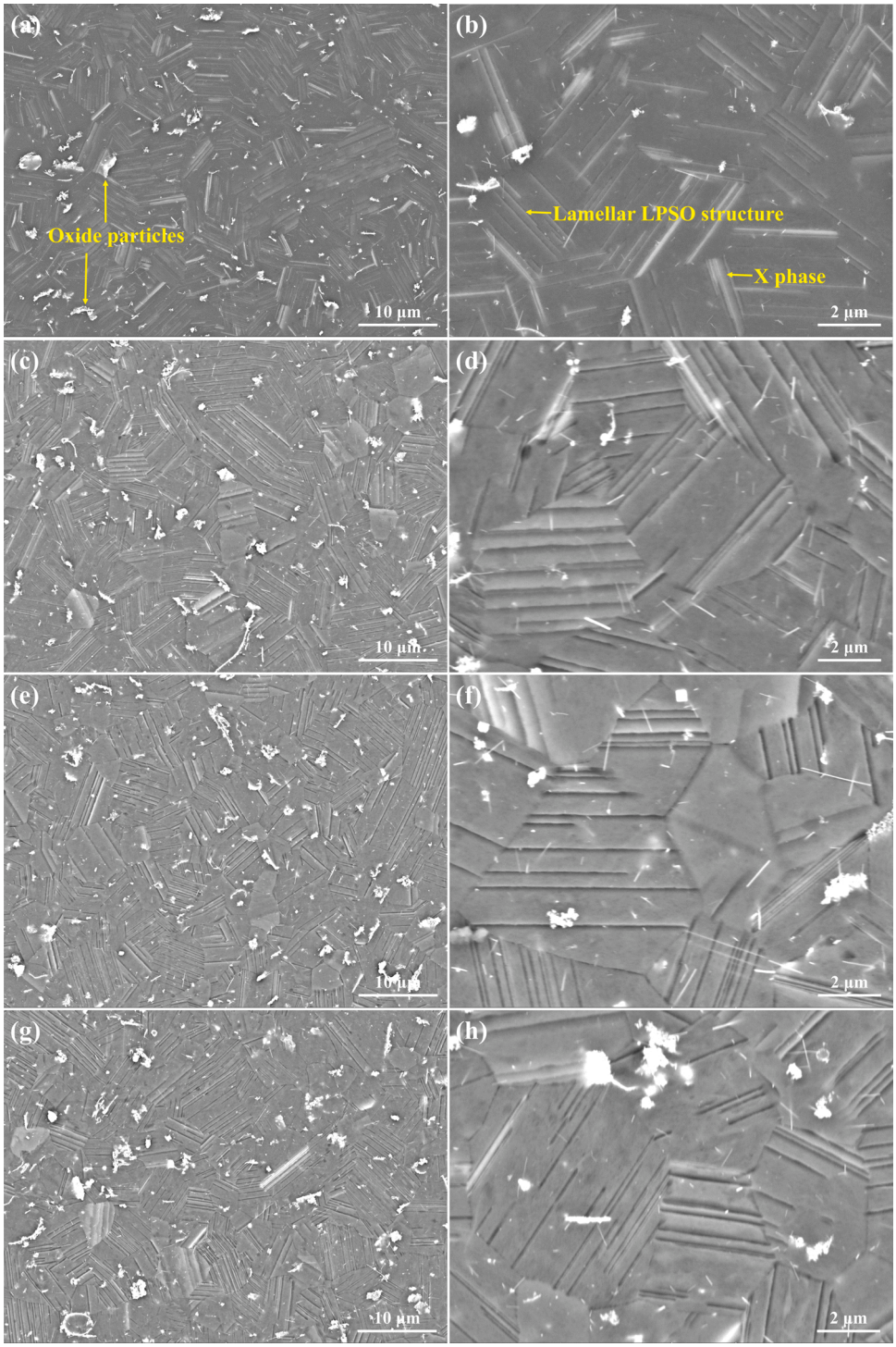

Fig. 8. BSE-SEM images of the as built GWZ1031K alloy solution treated at 500 ℃ for (a, b)1 h; (c, d)4 h; (e, f)8 h; (g, h)12 h.

treated GWZ1031K alloy at 450 ℃ for 12 h not only has relatively higher YS, but more importantly, has the highest EL. Therefore, the best solution treatment time at 450 ℃ for the as built GWZ1031K alloy is 12 h. The LPBF-T4–2 GWZ1031K alloy is defined as the as built GWZ1031K alloy solution treated at 450 ℃ for 12 h.

Fig. 12 illustrates the influence of solution temperature and treatment time on average grain size of solution-treated GWZ1031K alloys. As the solution temperature or treatment time increases, grain growth is inevitable. The grain growth of solution-treated GWZ1031K alloy at 500 ℃ is more obvious than that at 450 ℃. The average grain sizes of LPBF-T4–1 and LPBF-T4–2 GWZ1031K alloys are 4.6 ± 0.6 μm and 4.9 ± 0.8 μm, respectively, so the fine grains in the as built state are well retained under the optimized solution conditions. X phase at the grain boundaries is a thermally stable phase, which can hinder grain growth during solution heat treatment [65].

Fig. 13 depicts bright-field TEM images and high resolution TEM (HRTEM) images of X phase and lamellar LPSO structure in the LPBF-T4 GWZ1031K alloy. The chemical compositions of the X phase and the lamellar LPSO structure measured by STEM/EDS are Mg-10.8 Gd-2.3 Y-6.2 Zn and Mg-11.0 Gd-2.4 Y-6.0 Zn (at%), respectively. This indicates that both X phase and lamellar LPSO structure are enriched in rare earth (Gd and Y) and Zn elements. Both lamellar LPSO structure and X phase

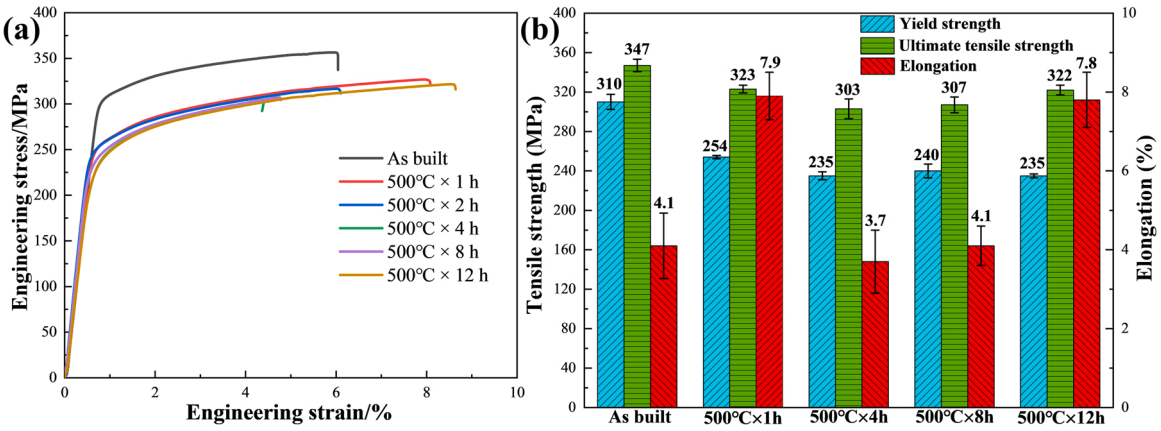

Fig. 9. Typical engineering stress-strain curves (a) and room temperature tensile properties (b) of the as built and solution-treated GWZ1031K alloy at 500 ℃ for different time.

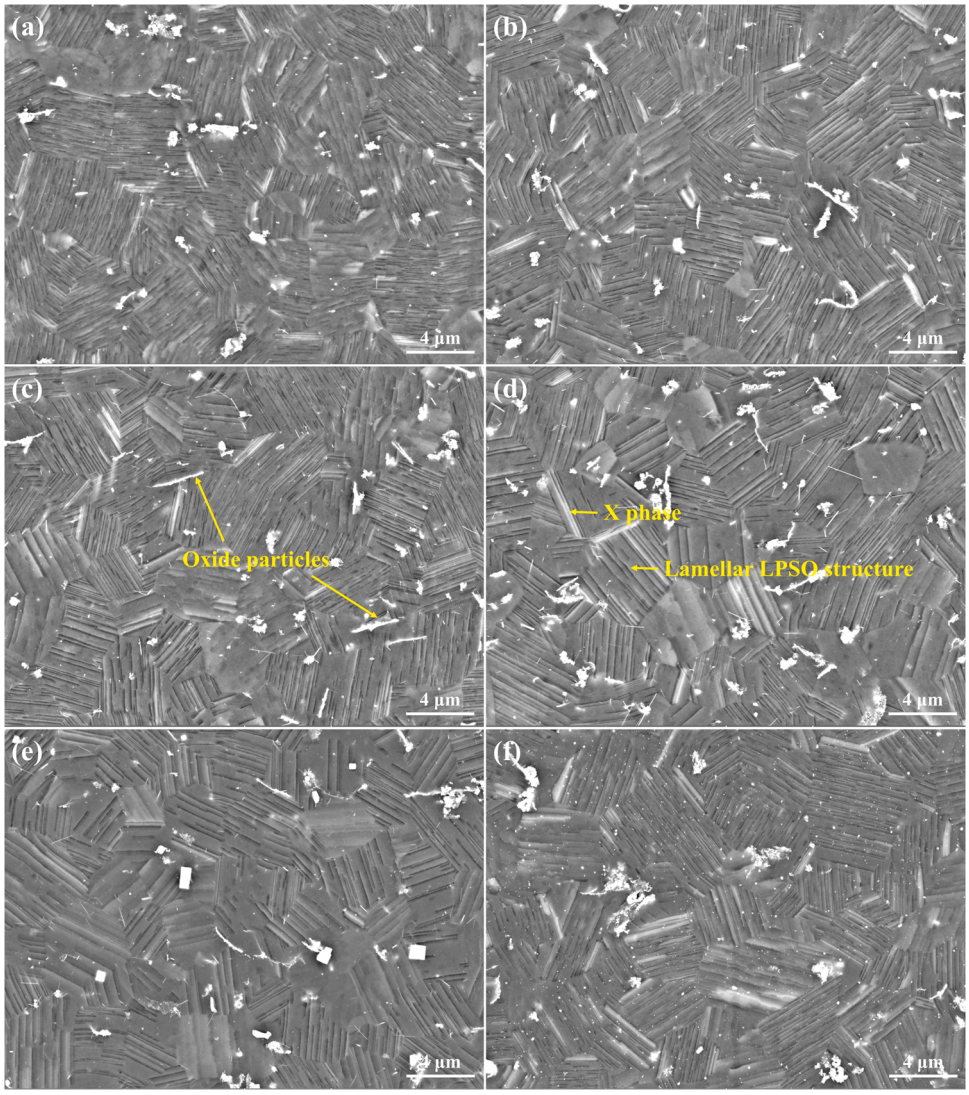

Fig. 10. BSE-SEM images of the as built GWZ1031K alloy solution treated at 450 ℃ for (a)1 h; (b)4 h; (c)8 h; (d)12 h; (e) 24 h; (f) 36 h.

exhibit typical characteristics of the 14 H-type LPSO structure (a=0.325 nm, c= 3.722 nm) [65]. There are 13 equally spaced spots represented by red arrows between the center spot and $(0002)_{Mg}$ spot in the selected area electron diffraction (SAED) patterns (Fig. 13c, f). In addition, uniformly distributed lattice fringes with a period length of 1.8 nm in HRTEM micrographs (Fig. 13b, e) also suggest the presence of 14 H-type LPSO structure [66,67]. Although the crystal structure, lattice parameter, and chemical composition of lamellar LPSO structure and X

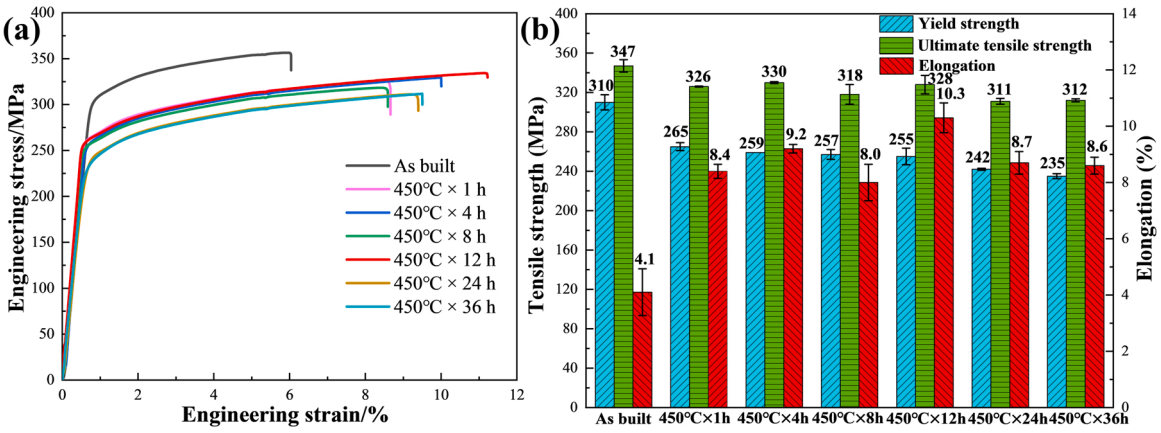

Fig. 11. Typical engineering stress-strain curves (a) and room temperature tensile properties (b) of the as built and solution-treated GWZ1031K alloy at 450 ℃ for different time.

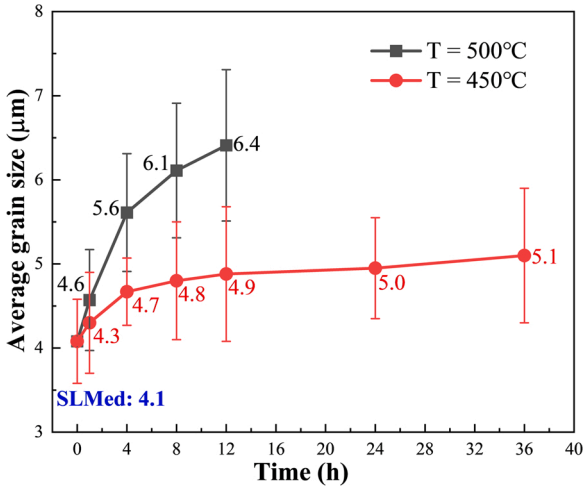

Fig. 12. The influence of solution temperature and treatment time on the average grain size.

phase are identical, for the convenience of distinguishing, the 14 H-LPSO structure inside grains and at grain boundaries are named as lamellar LPSO structure and X phase, respectively. During solution heat treatment, X phase is transformed from the eutectic phase while lamellar LPSO structure is precipitated from supersaturated α-Mg matrix owing to the enrichment of Gd and Zn elements. Additionally, 14 H-LPSO structure exists in the entire X phase at grain boundaries while 2 H-Mg and 14 H-LPSO are alternately distributed in the lamellar LPSO structure inside grains [54,65].

3.5. Aging hardening response and precipitates

Fig. 14 displays the aging hardening curves of the LPBF-T4 GWZ1031K alloy at aging temperatures of 175 ℃ and 200 ℃. The key values on the aging hardening curves are listed in Table 3. The hardness increases rapidly at the early stage due to the high super-saturation of alloying elements, indicating a strong aging hardening response of the LPBF-T4 GWZ1031K alloy. Although the peak-aged hardness at 200 ℃ is slightly lower than that at 175 ℃ (131.2 HV versus 132.5 HV), time to peak-aged hardness at 200 ℃ is significantly shorter than that at 175 ℃ (64 h versus 256 h), allowing for energy and time savings. Therefore, 200 ℃ × 64 h is selected as the aging condition for the LPBF-T4 GWZ1031K alloy. The LPBF-T6–1 and LPBF-T6–2 GWZ1031K alloys are respectively defined as the LPBF-T4–1 and LPBF-T4–2 GWZ1031K alloys aging treated at 200 ℃ for 64 h.

Fig. 15 displays bright-field TEM images and corresponding SAED patterns of the LPBF-T6 GWZ1031K alloy. After aging heat treatment, both SAED patterns (Fig. 15a, c) and morphology micrographs (Fig. 15c-d) confirm the existence of numerous aging precipitates including β′ and β_1 phases on the prismatic plane of the Mg matrix. The basal 14H-LPSO structure can hinder the growth of prismatic β′ precipitates along the $[0001]_\alpha$ direction (Fig. 15b), which contributes more to the tensile strengths than single prismatic precipitates [5]. Intensive β' aging precipitates containing three variants in a triangular arrangement are evenly distributed inside grains (Fig. 15c), which are the most important strengthening phase in Mg-Gd series alloys [68]. Furthermore, two β' precipitates are linked by one β_1 precipitate (Fig. 15c-d) to lower the shear strain energy around the β' precipitates [69].

3.6. Room temperature tensile properties

Fig. 16 shows the typical engineering stress-strain curves of the as built GWZ1031K alloy under different states. Table 4 summarizes the room temperature tensile properties of the as built and gravity cast [11] GWZ1031K alloys under different states. The as built alloy exhibits high strength and moderate ductility. As compared to gravity cast counterpart, the as built alloy not only achieves obviously higher YS (+146 MPa) and UTS (+128 MPa), but also retains slightly higher EL (+0.6%). A simple direct aging heat treatment at 175 ℃ for 64 h after LPBF leads to an ultra-high YS but a low EL in the LPBF-T5 alloy. On the one hand, a network of hard and brittle eutectic phases in the as built alloy remains unchanged during direct aging heat treatment, which causes crack initiation during tensile deformation leading to low EL. On the other hand, numerous aging precipitates induced by aging heat treatment usually result in a significant drop in EL [4,5,11]. The YS decreases, but EL improves remarkably after solution heat treatment. Both tensile strengths (YS and UTS) and ductility (EL) of LPBF-T4–2 alloy are better than that of LPBF-T4–1 alloy. Aging heat treatment can enhance tensile strengths significantly but deteriorate ductility obviously. Although the YS of LPBF-T6–1 alloy is slightly better than that of LPBF-T6–2 alloy (323 MPa versus 316 MPa), the EL of LPBF-T6–1 alloy is only half of LPBF-T6–2 alloy (1.0% versus 2.2%). In the LPBF-T4–2 alloy, the denser lamellar LPSO structure contributes more to EL but slightly reduces precipitation potential, resulting in slightly lower YS in the LPBF-T6–2 alloy. Compared with cast and cast-T6 alloys, as built and LPBF-T6 alloys have obviously higher tensile strengths and slightly higher ductility, suggesting that LPBF is an efficient method for fabricating high-performance Mg alloys. Unexpectedly, the room temperature tensile properties of LPBF-T4 and LPBF-T6 alloys are even similar to those of extruded and extruded-T5 alloys.

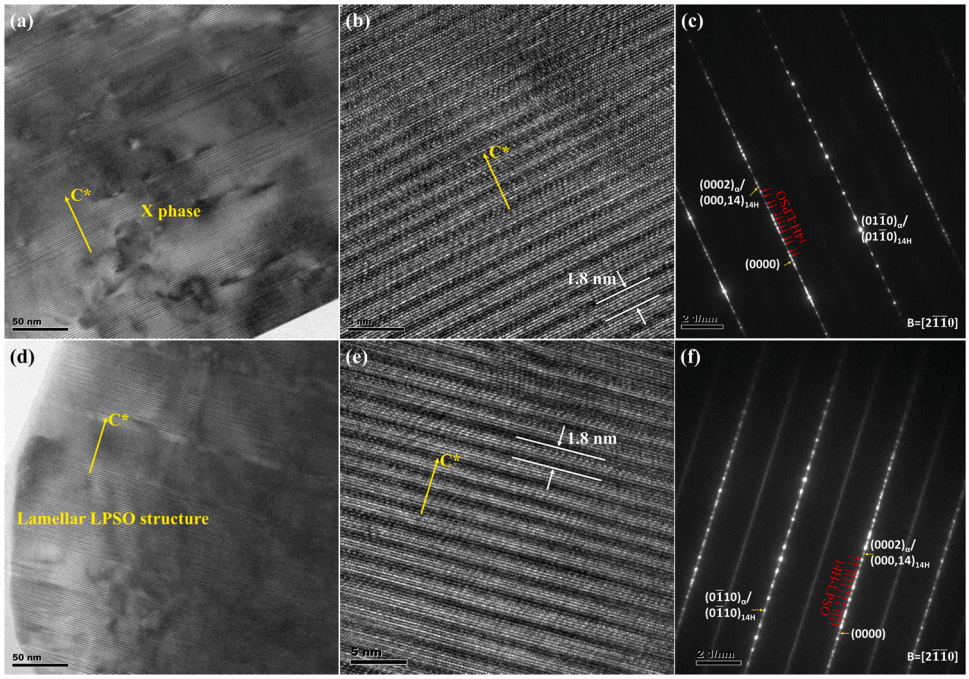

Fig. 13. Bright-field TEM images (a, d), HRTEM images (b, e), and SAED patterns (c, f) of X phase (a-c) and lamellar LPSO structure (d-f) in the LPBF-T4 GWZ1031K alloy. The incident electron beam was parallel to the $[2\bar{1}\bar{1}0]_\alpha$ direction.

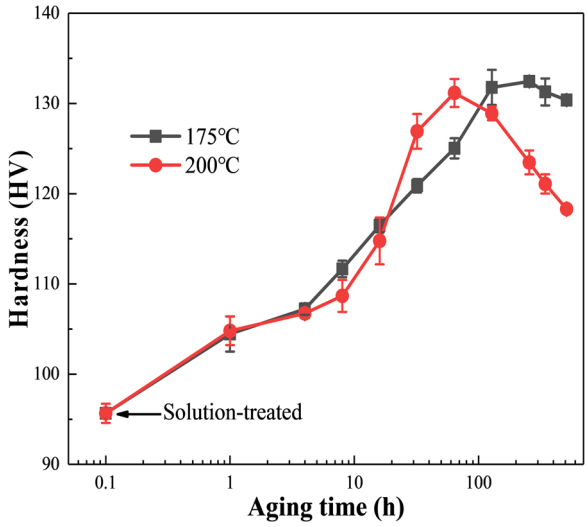

Fig. 14. The aging hardening curves of the LPBF-T4 GWZ1031K alloy at different aging temperatures.

Table 3
The key values on the aging hardening curves of the LPBF-T4 GWZ1031K alloy at different aging temperatures.

Aging temperature/℃	Initial hardness/HV	Peak-aged hardness/HV	Hardness increment/HV	Time to peak-aged hardness/h
175	95.7 ± 1.1	132.5 ± 0.4	36.8	256
200	95.7 ± 1.1	131.2 ± 1.0	35.5	64

4. Discussion

4.1. Unique microstructure of the as built GWZ1031K alloy

The experimental results indicate that the microstructure of the as built GWZ1031K alloy is extremely different from that of the traditional gravity cast alloy. Firstly, the as built alloy has extremely finer grains than cast alloy (4.1 μm versus 102 μm [11]). The average grain size of the as built alloy is even smaller than that of the extruded alloy (dynamically recrystallized grains of 8 μm [11]). Zhu et al. [40] found that the grains grow from 1 to 2 μm to 8–10 μm from the bottom to the top in one molten pool due to the change of temperature gradient and solidification rate in the as built AZ91D alloy. Fortunately, rapid solidification and addition of Zr element (0.4 wt% in the powder and 0.43 wt % in the as built alloy) for grain refinement contribute to fine and homogeneous grains in the as built GWZ1031K alloy [22]. Secondly, the as built and cast alloys have the same type of $(Mg,Zn)_3(Gd,Y)$ eutectic phase, but the as built alloy has less and finer eutectic phase than the cast alloy. The solute trapping effect [70] caused by laser rapid solidification increases the solid solubility of alloying elements and impedes the formation of the eutectic phase. Thirdly, there are lamellar 14 H-LPSO phases at the grain interior in the gravity cast alloy [11], whereas the lamellar 14 H-LPSO structure is not found in the as built alloy. This is due to the limiting effect of the high cooling rate of the LPBF process on the diffusion of alloying elements during solidification. Lastly, undesired yttrium oxides (Y_2O_3) originating from the oxide particles in powder and a residual small amount of oxygen in the build chamber are found with an area fraction of 1.67 ± 0.17% in the as built alloy, while almost no oxide inclusion exists in the cast alloy.

Liao et al. [71] noticed an unusual grain growth from 19 μm to 158 μm during solution heat treatment (525 ℃ × 4 h) of laser melting deposited GW103K alloy. However, after appropriate solution heat treatment, the LPBF-T4 GWZ1031K alloy retains the fine grains of the as built alloy while the hard and brittle eutectic phase transforms into a relatively soft and deformable LPSO structure [8]. The average grain size only increases from 4.1 μm in the as built state to 4.9 μm in the LPBF-T4–2 state because of a relatively low solution temperature of 450 ℃ and thermally stable X phase at grain boundaries. The coexistence of basal 14 H-LPSO structure and prismatic β′ and β_1 aging precipitates with relative perpendicular distribution is found in the LPBF-T6 GWZ1031K alloy, which is frequently discovered in cast-T6 Mg-Gd-(Y)-Zn-Zr alloys [5,15,72].

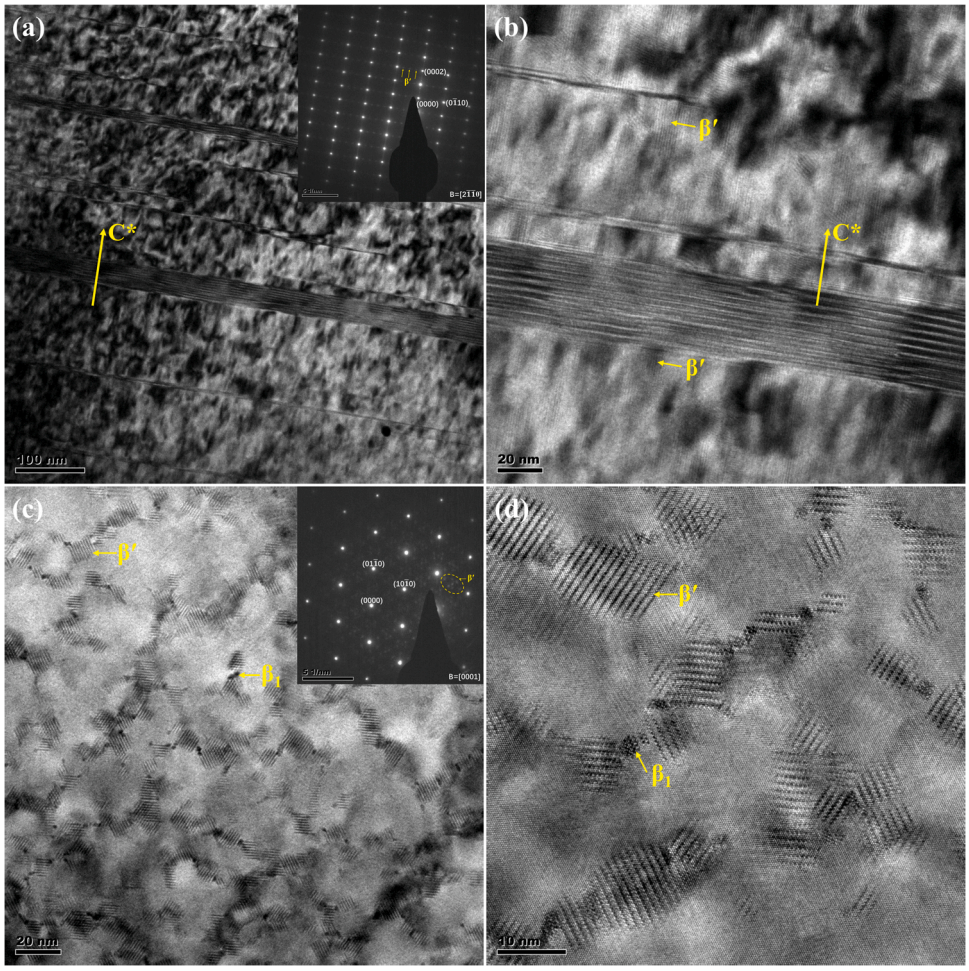

Fig. 15. Bright-field TEM images and corresponding SAED patterns of the LPBF-T6 GWZ1031K alloy. The incident electron beams were parallel to the $[2\bar{1}\bar{1}0]_\alpha$ direction in (a, b) and the $[0001]_\alpha$ direction in (c, d).

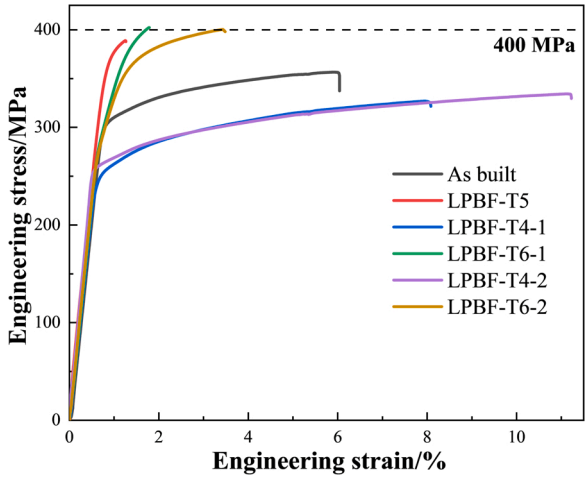

Fig. 16. Typical engineering stress-strain curves of the as built GWZ1031K alloy under different states.

4.2. *Unique mechanical properties of the as built GWZ1031K alloy*

Room temperature tensile properties of the as built and gravity cast GWZ1031K alloys under different states are compared in Fig. 16b and Table 4. Compared with its cast counterpart, the as built alloy not only has considerably higher YS (310 MPa versus 164 MPa, almost twice), but also has slightly higher EL (4.1% versus 3.5%). Both the fine grain strengthening (average grain size 4.1 μm versus 102 μm) and solid solution strengthening (the ultra-fast cooling rate leads to higher solid solubility of alloying elements with less and finer eutectic phase) are most probably responsible for the enhanced YS of the as built alloy. In addition, a network of eutectic phases on the grain boundaries can also strengthen the as built alloy. Fine grains and secondary eutectic phase help to improve ductility while flaky Y_2O_3 particles are detrimental. Compared with the as built alloy, precipitation strengthening from numerous aging precipitates further increases YS to 365 ± 12 MPa in the LPBF-T5 alloy. Solution heat treatment improves EL greatly from 4.1% to 10.3% although YS decreases slightly. The relatively high YS in

Table 4
The room temperature tensile properties of the as built and gravity cast [11] GWZ1031K alloys under different states.

States	YS/MPa	UTS/MPa	EL/%
As built	310 ± 8	347 ± 6	4.1 ± 0.8
LPBF-T5	365 ± 12	381 ± 8	0.8 ± 0.3
LPBF-T4–1	245 ± 2	323 ± 4	7.9 ± 0.6
LPBF-T6–1	323 ± 5	400 ± 2	1.0 ± 0.2
LPBF-T4–2	255 ± 8	328 ± 9	10.3 ± 0.5
LPBF-T6–2	316 ± 5	400 ± 7	2.2 ± 0.3
Cast	164	219	3.5
Cast-T6 (500 ℃ × 10 h + 225 ℃ × 32 h)	253	364	2.0
Extruded	231	347	11.0
Extruded-T5 (200 ℃ × 96 h)	339	428	4.0

the LPBF-T4 alloy comes from fine grain strengthening from an average grain size of 4.9 μm, secondary phase strengthening from X phase and lamellar LPSO structure, and solution strengthening from the dissolution of eutectic phase. On the contrary, aging heat treatment can enhance YS at the expense of EL. YS of LPBF-T6 alloy is also obviously superior to that of cast-T6 alloy (316 MPa versus 253 MPa), and EL of LPBF-T6 alloy is similar to that of cast-T6 alloy (2.2% versus 2%).

Table 5 lists the room temperature tensile properties of as built Mg alloys obtained in the present work and reported in the literature, and Fig. 17 presents a summary chart of UTS versus EL listed in Table 4 and Table 5. The room temperature tensile properties of the as built GWZ1031K alloy under different states located at the upper part of Fig. 17 are superior to the other as built Mg alloys. Among all reported as-built Mg alloys, the LPBF-T6 GWZ1031K alloy has the highest UTS of 400 MPa, making it a viable candidate for lightweight load-bearing components used in many critical engineering fields. The high tensile strengths of LPBF-T6 alloy can be explained with the help of the following four viewpoints. (1) The homogeneous and fine grains with an average grain size of 4.9 μm cause significant fine grain strengthening. (2) Densely distributed prismatic β′ and β_1 aging precipitates lead to significant precipitation strengthening. (3) The lamellar LPSO structure inside grains and X phase at grain boundaries, having larger hardness and Young's modulus than α-Mg matrix, result in secondary phase strengthening. (4) The coexistence of basal 14H-LPSO structure and prismatic β′ and β_1 aging precipitates with relative perpendicular distribution contributes to extra composite strengthening.

Unexpectedly, the room temperature tensile properties of the LPBF-T4 and LPBF-T6 GWZ1031K alloys are close to that of the extruded and extruded-T5 alloys, respectively. However, the microstructure of extruded and extruded-T5 alloys is refined by dynamic recrystallization during thermal plastic deformation at 400 ℃. The preparation process of extruded and extruded-T5 alloys involves several complicated steps (casting→heat treatment→extrusion→heat treatment), and only components having simple shapes can be fabricated by this method. In addition, deformation texture produced during extrusion often results in anisotropy of mechanical properties. On the contrary, the microstructure of the LPBF-T4 and LPBF-T6 GWZ1031K alloys is obtained by a solidification process that does not involve thermal plastic deformation, and the preparation process is relatively shorter (LPBF→heat treatment). Mechanical properties of the LPBF-T4 and LPBF-T6 GWZ1031K alloys are isotropic because of the uniform equiaxed grains. The LPBF can be used to prepare components of any complex shape with a precision of about 0.1 mm. Therefore, the LPBF process when combined with appropriate post-processing is a very promising technique for preparing high-performance Mg alloy components for engineering applications.

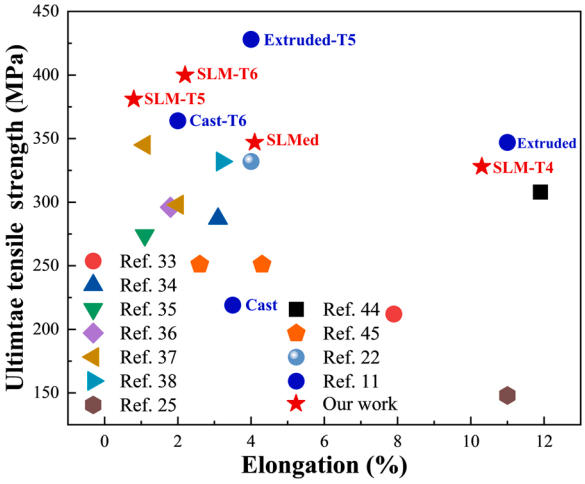

Fig. 17. A summary chart of UTS versus EL listed in Table 4 and Table 5.

5. Conclusions

A high-strength GWZ1031K alloy was manufactured by LPBF and post-processing. The microstructure and mechanical properties of the as built, LPBF-T4 and LPBF-T6 alloys were systematically investigated and compared with gravity cast alloys. The major findings of this study can be summarized as follows:

(1) The as built GWZ1031K alloy is composed of fine equiaxed α-Mg grains with an average grain size of 4.1 ± 0.5 μm, reticular β-$(Mg,Zn)_3(Gd,Y)$ eutectic phase and undesired Y_2O_3 oxide phase, which exhibits YS of 310 ± 8 MPa, UTS of 347 ± 6 MPa and EL of 4.1 ± 0.8%. Compared with its cast counterpart, the as built alloy has significantly refined grains and eutectic phase contributing to obviously higher tensile strengths and slightly higher ductility.
(2) Direct aging heat treatment after LPBF leads to an ultra-high YS of 365 MPa but a low EL of 0.8% in the LPBF-T5 alloy.
(3) Solution heat treatment transforms the hard and brittle eutectic phase into the relatively soft and deformable lamellar LPSO structure inside grains and X phase at grain boundaries without

Table 5
The room temperature tensile properties of the as built Mg alloys obtained in the present work and reported in the literature.

Materials system	Chemical compositions (wt%)	States	Tensile properties			Ref.
			YS/MPa	UTS/MPa	EL/%	
GWZ1031K	Mg-9.86Gd-2.35Y-0.96Zn-0.40Zr	As built	310	347	4.1	Present work
		LPBF-T5	365	381	0.8	
		LPBF-T4	255	328	10.3	
		LPBF-T6	316	400	2.2	
AZ31B	Mg-2.97Al-0.89Zn	As built	183	212	7.9	[33]
AZ61	Mg-6.25Al-1.24Zn-0.27Mn	As built	233	287	3.1	[34]
A9	Mg-9Al	As built	–	274	1.1	[35]
AZ91D	Mg-8.95Al-0.44Zn-0.19Mn	As built	254	296	1.8	[36]
AZ91D	Mg-9.08Al-0.65Zn-0.23Mn	As built	265	298	2.0	[37]
AZ91D+ 5vol%SiCnp	Mg-9.08Al-0.65Zn-0.23Mn+ 5vol%SiCnp	As built	308	345	1.1	
AZX912	Mg-8.55Al-0.64Zn-1.81Ca-0.18Mn	As built	253	332	3.2	[38]
Z1	Mg-1Zn	As built	–	148	11.0	[25]
WE43	Mg-3.48Y-1.62Nd-0.71Gd-0.40Zr	As built	296	308	11.9	[44]
WE43	Mg-3.7–4.3Y-2.4–4.4RE-0.40Zr	As built	215	251	2.6	[45]
		LPBF-T6	219	251	4.3	
GZ112K	Mg-11.82Gd-2.03Zn-0.43Zr	As built	325	332	4.0	[22]

- represents not reported.

obvious grain growth, which results in a significant increase in ductility. The LPBF-T4 GWZ1031K alloy exhibits YS of 255 ± 8 MPa, UTS of 328 ± 9 MPa, and EL of 10.3 ± 0.5%.

(4) The LPBF-T6 GWZ1031K alloy is composed of basal 14 H-LPSO structure and prismatic β′ and β_1 aging precipitates with the relative perpendicular distribution. The YS, UTS and EL of the LPBF-T6 alloy are 316 ± 5 MPa, 400 ± 7 MPa, and 2.2 ± 0.3%, respectively.

CRediT authorship contribution statement

Qingchen Deng: Conceptualization, Data curation, Formal analysis, Investigation, Methodology, Validation, Writing – original draft, Writing – review & editing. **Yujuan Wu:** Writing – review & editing, Validation, Supervision, Funding acquisition. **Qianye Wu:** Writing – review & editing. **Yanting Xue:** Writing – review & editing. **Yu Zhang:** Writing – review & editing. **Liming Peng:** Supervision, Funding acquisition, Resources, Project administration. **Wenjiang Ding:** Supervision, Funding acquisition, Resources.

Declaration of Competing Interest

The authors declare that they have no known competing financial interests or personal relationships that could have appeared to influence the work reported in this paper.

Acknowledgements

This work was funded by the National Natural Science Foundation of China (Nos. 51971130, 51771113, 51821001, 51901027) and the High Technology and Key Development Project of Ningbo, China (No. 2019B10102).

References

[1] P. Fu, L. Peng, H. Jiang, W. Ding, C. Zhai, Tensile properties of high strength cast Mg alloys at room temperature: a review, China Foundry 11 (2014) 277–286.
[2] G. Wu, C. Wang, M. Sun, W. Ding, Recent developments and applications on high-performance cast magnesium rare-earth alloys, J. Magnes. Alloy. 9 (2021) 1–20.
[3] Y. Yang, C. He, E. Dianyu, W. Yang, F. Qi, D. Xie, L. Shen, S. Peng, C. Shuai, Mg bone implant: features, developments and perspectives, Mater. Des. 185 (2020), 108259.
[4] Y. Zhang, Y. Wu, L. Peng, P. Fu, F. Huang, W. Ding, Microstructure evolution and mechanical properties of an ultra-high strength casting Mg–15.6Gd–1.8Ag–0.4Zr alloy, J. Alloy. Compd. 615 (2014) 703–711.
[5] W. Rong, Y. Wu, Y. Zhang, M. Sun, J. Chen, L. Peng, W. Ding, Characterization and strengthening effects of γ′ precipitates in a high-strength casting Mg-15Gd-1Zn-0.4Zr (wt%) alloy, Mater. Charact. 126 (2017) 1–9.
[6] X. Xue, Y. Wu, N. Su, X. Heng, Q. Deng, Z. Chang, L. Peng, High-strength GWZ1031K alloy with gradient structure induced by surface mechanical attrition treatment, Mater. Charact. 170 (2020), 110701.
[7] N. Su, X. Xue, H. Zhou, Y. Wu, Q. Deng, K. Yang, Q. Chen, B. Chen, L. Peng, Effects of nanoprecipitates and LPSO structure on deformation and fracture behaviour of high-strength Mg-Gd-Y-Zn-Mn alloys, Mater. Charact. 165 (2020), 110396.
[8] N. Su, Y. Wu, Y. Zhang, X. Cheng, L. Peng, K. Yang, Q. Chen, Microstructure evolution difference in Mg96.5Gd2.5Zn1 alloys extruded from as-cast and solution-treated states, J. Mater. Process. Technol. 282 (2020), 116666.
[9] N. Su, Y. Wu, Q. Deng, Z. Chang, Q. Wu, Y. Xue, K. Yang, Q. Chen, L. Peng, Synergic effects of Gd and Y contents on the age-hardening response and elevated-temperature mechanical properties of extruded Mg–Gd(-Y)-Zn-Mn alloys, Mater. Sci. Eng. A 810 (2021), 141019.
[10] M. Qian, D.H. StJohn, M.T. Frost, Characteristic zirconium-rich coring structures in Mg–Zr alloys, Scr. Mater. 46 (2002) 649–654.
[11] X.B. Liu, R.S. Chen, E.H. Han, Effects of ageing treatment on microstructures and properties of Mg–Gd–Y–Zr alloys with and without Zn additions, J. Alloy. Compd. 465 (2008) 232–238.
[12] J.P. Weiler, A review of magnesium die-castings for closure applications, J. Magnes. Alloy. 7 (2019) 297–304.
[13] Y. Zhang, W. Rong, Y. Wu, L. Peng, J.-F. Nie, N. Birbilis, A comparative study of the role of Ag in microstructures and mechanical properties of Mg-Gd and Mg-Y alloys, Mater. Sci. Eng. A 731 (2018) 609–622.
[14] J. Li, Z. He, P. Fu, Y. Wu, L. Peng, W. Ding, Heat treatment and mechanical properties of a high-strength cast Mg–Gd–Zn alloy, Mater. Sci. Eng. A 651 (2016) 745–752.
[15] D. Wang, P. Fu, L. Peng, Y. Wang, W. Ding, Development of high strength sand cast Mg–Gd–Zn alloy by co-precipitation of the prismatic β′ and β1 phases, Mater. Charact. 153 (2019) 157–168.
[16] L. Jiang, W. Liu, G. Wu, W. Ding, Effect of chemical composition on the microstructure, tensile properties and fatigue behavior of sand-cast Mg–Gd–Y–Zr alloy, Mater. Sci. Eng. A 612 (2014) 293–301.
[17] T. Kurzynowski, A. Pawlak, I. Smolina, The potential of SLM technology for processing magnesium alloys in aerospace industry, Arch. Civ. Mech. Eng. 20 (2020).
[18] S. Liu, H. Guo, A review of SLMed magnesium alloys: processing, properties, alloying elements and postprocessing, Metals 10 (2020) 1073.
[19] K.G. Prashanth, S. Scudino, H.J. Klauss, K.B. Surreddi, L. Löber, Z. Wang, A. K. Chaubey, U. Kühn, J. Eckert, Microstructure and mechanical properties of Al–12Si produced by selective laser melting: effect of heat treatment, Mater. Sci. Eng. A 590 (2014) 153–160.
[20] C.C. Ng, M.M. Savalani, M.L. Lau, H.C. Man, Microstructure and mechanical properties of selective laser melted magnesium, Appl. Surf. Sci. 257 (2011) 7447–7454.
[21] K. Wei, M. Gao, Z. Wang, X. Zeng, Effect of energy input on formability, microstructure and mechanical properties of selective laser melted AZ91D magnesium alloy, Mater. Sci. Eng. A 611 (2014) 212–222.
[22] Q. Deng, Y. Wu, Y. Luo, N. Su, X. Xue, Z. Chang, Q. Wu, Y. Xue, L. Peng, Fabrication of high-strength Mg-Gd-Zn-Zr alloy via selective laser melting, Mater. Charact. 165 (2020), 110377.
[23] L. Zhuo, Z. Wang, H. Zhang, E. Yin, Y. Wang, T. Xu, C. Li, Effect of post-process heat treatment on microstructure and properties of selective laser melted AlSi10Mg alloy, Mater. Lett. 234 (2019) 196–200.
[24] J. Liu, B. Yin, Z. Sun, P. Wen, Y. Zheng, Y. Tian, Hot cracking in ZK60 magnesium alloy produced by laser powder bed fusion process, Mater. Lett. 301 (2021), 130283.
[25] K. Wei, X. Zeng, Z. Wang, J. Deng, M. Liu, G. Huang, X. Yuan, Selective laser melting of Mg-Zn binary alloys: Effects of Zn content on densification behavior, microstructure, and mechanical property, Mater. Sci. Eng. A 756 (2019) 226–236.
[26] S. Liu, H. Guo, Influence of hot isostatic pressing (HIP) on mechanical properties of magnesium alloy produced by selective laser melting (SLM), Mater. Lett. 265 (2020), 127463.
[27] X.P. Li, G. Ji, Z. Chen, A. Addad, Y. Wu, H.W. Wang, J. Vleugels, J. Van Humbeeck, J.P. Kruth, Selective laser melting of nano-TiB 2 decorated AlSi10Mg alloy with high fracture strength and ductility, Acta Mater. 129 (2017) 183–193.
[28] L. Thijs, F. Verhaeghe, T. Craeghs, J.V. Humbeeck, J.-P. Kruth, A study of the microstructural evolution during selective laser melting of Ti–6Al–4V, Acta Mater. 58 (2010) 3303–3312.
[29] Y. Gao, D. Zhang, M. Cao, R. Chen, Z. Feng, R. Poprawe, J.H. Schleifenbaum, S. Ziegler, Effect of δ phase on high temperature mechanical performances of Inconel 718 fabricated with SLM process, Mater. Sci. Eng. A 767 (2019).
[30] Y.M. Wang, T. Voisin, J.T. McKeown, J. Ye, N.P. Calta, Z. Li, Z. Zeng, Y. Zhang, W. Chen, T.T. Roehling, R.T. Ott, M.K. Santala, P.J. Depond, M.J. Matthews, A. V. Hamza, T. Zhu, Additively manufactured hierarchical stainless steels with high strength and ductility, Nat. Mater. 17 (2018) 63–71.
[31] X. Niu, H. Shen, J. Fu, J. Yan, Y. Wang, Corrosion behaviour of laser powder bed fused bulk pure magnesium in hank's solution, Corros. Sci. 157 (2019) 284–294.
[32] Christian Matthias Gieseke, Stefan Noelke, Volker Kaierle, H. Wesling, Haferkamp, selective laser melting of magnesium and magnesium alloys, Magnes. Technol. 2013 (2013) 65–68.
[33] A. Pawlak, P.E. Szymczyk, T. Kurzynowski, E. Chlebus, Selective laser melting of magnesium AZ31B alloy powder, Rapid Prototyp. J. 26 (2019) 249–258.
[34] S. Liu, W. Yang, X. Shi, B. Li, S. Duan, H. Guo, J. Guo, Influence of laser process parameters on the densification, microstructure, and mechanical properties of a selective laser melted AZ61 magnesium alloy, J. Alloy. Compd. 808 (2019), 151160.
[35] X. Niu, H. Shen, J. Fu, Microstructure and mechanical properties of selective laser melted Mg-9 wt%Al powder mixture, Mater. Lett. 221 (2018) 4–7.
[36] K. Wei, M. Gao, Z. Wang, X. Zeng, Effect of energy input on formability, microstructure and mechanical properties of selective laser melted AZ91D magnesium alloy, Mater. Sci. Eng. A 611 (2014) 212–222.
[37] X. Niu, H. Shen, J. Fu, J. Feng, Effective control of microstructure evolution in AZ91D magnesium alloy by SiC nanoparticles in laser powder-bed fusion, Mater. Des. 206 (2021), 109787.
[38] B. Proaño, H. Miyahara, T. Matsumoto, S. Hamada, H. Sakai, K. Ogawa, H. Suyalatu, Noguchi, Weakest region analysis of non-combustible Mg products fabricated by selective laser melting, Theor. Appl. Fract. Mech. 103 (2019), 102291.
[39] C. He, S. Bin, P. Wu, C. Gao, P. Feng, Y. Yang, L. Liu, Y. Zhou, M. Zhao, S. Yang, C. Shuai, Microstructure evolution and biodegradation behavior of laser rapid solidified Mg–Al–Zn alloy, Metals 7 (2017).
[40] Z. Zhu, M. Zhang, C. Chen, Effect of selective laser melting on microstructure and properties of AZ91D alloy, Mater. Sci. Eng. Technol. 50 (2019) 1484–1494.
[41] K. Wei, Z. Wang, X. Zeng, Influence of element vaporization on formability, composition, microstructure, and mechanical performance of the selective laser melted Mg–Zn–Zr components, Mater. Lett. 156 (2015) 187–190.
[42] C. Shuai, Y. Yang, P. Wu, X. Lin, Y. Liu, Y. Zhou, P. Feng, X. Liu, S. Peng, Laser rapid solidification improves corrosion behavior of Mg-Zn-Zr alloy, J. Alloy. Compd. 691 (2017) 961–969.
[43] Y. Yang, C. Lu, L. Shen, Z. Zhao, S. Peng, C. Shuai, In-situ deposition of apatite layer to protect Mg-based composite fabricated via laser additive manufacturing,

Journal of Magnesium and Alloys ⟨https://doi.org/10.1016/j.jma.2021.1004.1009⟩.
[44] N.A. Zumdick, L. Jauer, L.C. Kersting, T.N. Kutz, J.H. Schleifenbaum, D. Zander, Additive manufactured WE43 magnesium: a comparative study of the microstructure and mechanical properties with those of powder extruded and as-cast WE43, Mater. Charact. 147 (2019) 384–397.
[45] H. Hyer, L. Zhou, G. Benson, B. McWilliams, K. Cho, Y. Sohn, Additive manufacturing of dense WE43 Mg alloy by laser powder bed fusion, Addit. Manuf. 33 (2020), 101123.
[46] S. Gangireddy, B. Gwalani, K. Liu, E.J. Faierson, R.S. Mishra, Microstructure and mechanical behavior of an additive manufactured (AM) WE43-Mg alloy, Addit. Manuf. 26 (2019) 53–64.
[47] F. Bar, L. Berger, L. Jauer, G. Kurtuldu, R. Schaublin, J.H. Schleifenbaum, J. F. Loffler, Laser additive manufacturing of biodegradable magnesium alloy WE43: a detailed microstructure analysis, Acta Biomater. 98 (2019) 36–49.
[48] Y. Li, J. Zhou, P. Pavanram, M.A. Leeflang, L.I. Fockaert, B. Pouran, N. Tumer, K. U. Schroder, J.M.C. Mol, H. Weinans, H. Jahr, A.A. Zadpoor, Additively manufactured biodegradable porous magnesium, Acta Biomater. 67 (2018) 378–392.
[49] Y. Wang, H. Huang, G. Jia, H. Zeng, G. Yuan, Fatigue and dynamic biodegradation behavior of additively manufactured Mg scaffolds, Acta Biomater. 135 (2021) 705–722.
[50] Y. Wang, P. Fu, N. Wang, L. Peng, B. Kang, H. Zeng, G. Yuan, W. Ding, Challenges and solutions for the additive manufacturing of biodegradable magnesium implants, Engineering 6 (2020) 1267–1275.
[51] Y. Yang, M. Yang, C. He, F. Qi, D. Wang, S. Peng, C. Shuai, Rare earth improves strength and creep resistance of additively manufactured Zn implants, Compos. Part B: Eng. 216 (2021), 108882.
[52] W. Zhang, L. Wang, Z. Feng, Y. Chen, Research progress on selective laser melting (SLM) of magnesium alloys: a review, Optik 207 (2020), 163842.
[53] Q. Deng, Y. Wu, N. Su, Z. Chang, J. Chen, L. Peng, W. Ding, Influence of friction stir processing and aging heat treatment on microstructure and mechanical properties of selective laser melted Mg-Gd-Zr alloy, Addit. Manuf. 44 (2021), 102036.
[54] Q. Deng, Y. Wu, W. Zhu, K. Chen, D. Liu, L. Peng, W. Ding, Effect of heat treatment on microstructure evolution and mechanical properties of selective laser melted Mg-11Gd-2Zn-0.4Zr alloy, Mater. Sci. Eng.: A 829 (2022), 142139.
[55] M. Zheng, L. Wei, J. Chen, Q. Zhang, C. Zhong, X. Lin, W. Huang, A novel method for the molten pool and porosity formation modelling in selective laser melting, Int. J. Heat Mass Transf. 140 (2019) 1091–1105.
[56] X. Shi, H. Wang, W. Feng, Y. Zhang, S. Ma, J. Wei, The crack and pore formation mechanism of Ti–47Al–2Cr–2Nb alloy fabricated by selective laser melting, Int. J. Refract. Met. Hard Mater. 91 (2020), 105247.
[57] P. Gao, W. Huang, H. Yang, G. Jing, Q. Liu, G. Wang, Z. Wang, X. Zeng, Cracking behavior and control of β-solidifying Ti-40Al-9V-0.5Y alloy produced by selective laser melting, J. Mater. Sci. Technol. 39 (2020) 144–154.
[58] H. Zhang, H. Zhu, X. Nie, J. Yin, Z. Hu, X. Zeng, Effect of Zirconium addition on crack, microstructure and mechanical behavior of selective laser melted Al-Cu-Mg alloy, Scr. Mater. 134 (2017) 6–10.
[59] R. Li, M. Wang, Z. Li, P. Cao, T. Yuan, H. Zhu, Developing a high-strength Al-Mg-Si-Sc-Zr alloy for selective laser melting: Crack-inhibiting and multiple strengthening mechanisms, Acta Mater. 193 (2020) 83–98.
[60] Y. Wang, L. Peng, Y. Ji, X. Cheng, C. Wang, Y. Wu, Y. Fu, L.-Q. Chen, Effect of cooling rates on the dendritic morphology transition of Mg–6Gd alloy by in situ X-ray radiography, J. Mater. Sci. Technol. 34 (2018) 1142–1148.
[61] D.H. StJohn, M. Qian, M.A. Easton, P. Cao, The Interdependence Theory: the relationship between grain formation and nucleant selection, Acta Mater. 59 (2011) 4907–4921.
[62] J.F. Nie, K. Oh-ishi, X. Gao, K. Hono, Solute segregation and precipitation in a creep-resistant Mg–Gd–Zn alloy, Acta Mater. 56 (2008) 6061–6076.
[63] W. Wang, L. He, X. Yang, D. Wang, Microstructure and microhardness mechanism of selective laser melting Mg-Y-Sm-Zn-Zr alloy, J. Alloy. Compd. 868 (2021), 159107.
[64] J. Fiocchi, A. Tuissi, C.A. Biffi, Heat treatment of aluminium alloys produced by laser powder bed fusion: a review, Mater. Des. 204 (2021), 109651.
[65] Y.J. Wu, X.Q. Zeng, D.L. Lin, L.M. Peng, W.J. Ding, The microstructure evolution with lamellar 14H-type LPSO structure in an Mg96.5Gd2.5Zn1 alloy during solid solution heat treatment at 773K, J. Alloy. Compd. 477 (2009) 193–197.
[66] Y.M. Zhu, M. Weyland, A.J. Morton, K. Oh-ishi, K. Hono, J.F. Nie, The building block of long-period structures in Mg–RE–Zn alloys, Scr. Mater. 60 (2009) 980–983.
[67] D. Wang, H. Wu, R. Wu, Y. Wang, J. Zhang, S. Betsofen, B. Krit, L. Hou, T. Nodir, The transformation of LPSO type in Mg-4Y–2Er-2Zn-0.6Zr and its response to the mechanical properties and damping capacities, J. Magnes. Alloy. 8 (2020) 793–798.
[68] J.F. Nie, Precipitation and hardening in magnesium alloys, Metall. Mater. Trans. A 43 (2012) 3891–3939.
[69] Y. Zhang, W. Rong, Y. Wu, L. Peng, J.-F. Nie, N. Birbilis, A detailed HAADF-STEM study of precipitate evolution in Mg–Gd alloy, J. Alloy. Compd. 777 (2019) 531–543.
[70] M.J. Aziz, Model for solute redistribution during rapid solidification, J. Appl. Phys. 53 (1982) 1158–1168.
[71] H. Liao, P. Fu, L. Peng, J. Li, S. Zhang, G. Hu, W. Ding, Microstructure and mechanical properties of laser melting deposited GW103K Mg-RE alloy, Mater. Sci. Eng. A 687 (2017) 281–287.
[72] D. Wang, P. Fu, L. Peng, Y. Wang, W. Ding, A study of microstructure, mechanical behavior and strengthen mechanism in the Mg-10Gd-0.2Zn-(Y)-0.4Zr alloy, Mater. Sci. Eng. A 793 (2020), 139881.